

A PARAMETRIC FINITE ELEMENT METHOD FOR SOLID-STATE
DEWETTING PROBLEMS IN THREE DIMENSIONS*QUAN ZHAO[†], WEI JIANG[‡], AND WEIZHU BAO[†]

Abstract. We propose a parametric finite element method (PFEM) for efficiently solving the morphological evolution of solid-state dewetting of thin films on a flat rigid substrate in three dimensions (3D). The interface evolution of the dewetting problem in 3D is described by a sharp-interface model, which includes surface diffusion coupled with contact line migration. A variational formulation of the sharp-interface model is presented, and a PFEM is proposed for spatial discretization. For temporal discretization, at each time step, we first update the position of the contact line according to the relaxed contact angle condition; then, by using the position of the new contact line as the boundary condition, we solve a linear system resulting from the discretization of PFEM to obtain the new surface at the next step. The well-posedness of the solution of the PFEM is also established. Extensive numerical results are reported to demonstrate the accuracy and efficiency of the proposed PFEM and to show the complexities of the dewetting morphology evolution observed in solid-state dewetting experiments.

Key words. solid-state dewetting, surface diffusion, moving contact line, sharp-interface model, Cahn–Hoffman ξ -vector

AMS subject classifications. 74H15, 74S05, 74M15, 65Z99

DOI. 10.1137/19M1281666

1. Introduction. Solid-state dewetting is a ubiquitous phenomenon in materials science, and it describes the agglomeration of solid thin films into arrays of isolated particles on a substrate (see, e.g., the review papers [48, 35]). In recent years, solid-state dewetting has found wide applications in thin film technologies, and it can be used to produce the controlled formation of an array of nanoscale particles, e.g., used in sensors [37] and as catalysts for carbon [43] and semiconductor nanowire growth [45]. Recently, it has attracted extensive attention of many research groups and has been widely studied from the experimental (e.g., [55, 56, 1, 42, 39, 34]) and theoretical (e.g., [46, 51, 17, 27, 49, 28, 5, 33, 60]) points of view.

The dewetting of thin solid films deposited on substrates is similar to the dewetting phenomena of liquid films. Although liquid-state wetting/dewetting problems have been extensively studied in fluid mechanics (e.g., [15, 41, 52, 53]), solid-state dewetting problems (i.e., surface diffusion-controlled geometric evolution) pose a considerable challenge in materials science, applied mathematics, and scientific computing. The major challenge comes from the difference of their mass transports. In general, surface diffusion has been recognized as the dominant mass transport for

*Submitted to the journal's Computational Methods in Science and Engineering section August 19, 2019; accepted for publication (in revised form) December 13, 2019; published electronically February 18, 2020.

<https://doi.org/10.1137/19M1281666>

Funding: The first author's research was supported by the Ministry of Education of Singapore grant R-146-000-247-114. The second author's research was supported by the National Natural Science Foundation of China through grant 11871384 and by the Natural Science Foundation of Hubei Province through grant 2019CFA007. The third author's research was supported by the Ministry of Education of Singapore grant R-146-000-296-112 (MOE2019-T2-1-063) and the National Natural Science Foundation of China grant 91630207.

[†]Department of Mathematics, National University of Singapore, Singapore 119076 (quanzhao90@nus.edu; matbaowz@nus.edu.sg, <http://blog.nus.edu.sg/matbwz/>).

[‡]Corresponding author. School of Mathematics and Statistics & Hubei Key Laboratory of Computational Science, Wuhan University, Wuhan, 430072, P.R. China (jiangwei1007@whu.edu.cn).

solid-state dewetting and has played an essential role in determining the morphology evolution of solid thin films during the dewetting. The surface diffusion equation for the evolution of a solid film with isotropic surface energy (i.e., a constant, labeled as γ_0) was given by Mullins [38]:

$$(1.1) \quad v_n = B\gamma_0\Delta_s \mathcal{H}, \quad \text{with } B = \frac{D_s\nu\Omega_0^2}{k_B T},$$

where v_n is the normal velocity of the film/vapor interface (surface), D_s is the surface diffusivity, $k_B T$ is the thermal energy, ν is the number of diffusing atoms per unit area, Ω_0 is the atomic volume, Δ_s is the Laplace–Beltrami operator, and \mathcal{H} represents the mean curvature of the interface. For anisotropic surface energy (i.e., a function, labeled as $\gamma = \gamma(\mathbf{n})$ with $\mathbf{n} = (n_1, n_2, n_3)^T$ representing the unit outward normal orientation of the interface), it means that the surface energy (density) exhibits dependence on the crystalline orientation, and (1.1) can be readily extended to the anisotropic case by replacing the mean curvature \mathcal{H} with the weighted mean curvature \mathcal{H}_γ as [47, 14]

$$(1.2) \quad \mathcal{H}_\gamma = \nabla_s \cdot \boldsymbol{\xi},$$

where ∇_s is the surface gradient operator, and $\boldsymbol{\xi} := \boldsymbol{\xi}(\mathbf{n})$ is well known as the Cahn–Hoffman $\boldsymbol{\xi}$ -vector [13, 24, 29, 30] which can be defined based on the homogeneous extension of $\gamma(\mathbf{n})$ as

$$(1.3) \quad \boldsymbol{\xi}(\mathbf{n}) = \nabla \hat{\gamma}(\mathbf{p}) \Big|_{\mathbf{p}=\mathbf{n}}, \quad \text{with } \hat{\gamma}(\mathbf{p}) = |\mathbf{p}| \gamma \left(\frac{\mathbf{p}}{|\mathbf{p}|} \right), \quad \forall \mathbf{p} \in \mathbb{R}^3 \setminus \{\mathbf{0}\},$$

with $|\mathbf{p}| := \sqrt{p_1^2 + p_2^2 + p_3^2}$, and $\mathbf{p} = (p_1, p_2, p_3)^T \in \mathbb{R}^3$.

Numerical simulations of geometric evolution equations (e.g., surface diffusion) have attracted considerable interest over the decades, and different methods have been proposed in the literature for simulating the evolution of a closed curve/surface under mean curvature flow, surface diffusion, Willmore flow, etc. For example, stable finite element methods for solving the flows of graphs [2, 16, 54] have been well studied. Unfortunately, these methods cannot be directly applied to the general curve/surface evolution due to complicated governing equations and geometric changes. Other front-tracking methods have been proposed to simulate evolutions for curves/surfaces, such as the marker-particle method [18, 36, 25] and the parametric finite element method (PFEM) [19, 3, 40, 21, 22]. These methods are very efficient and render a very accurate representation of the interface compared to the phase-field or level-set methods. However, throughout practical simulations, these algorithms generally need complicated mesh regularizations or frequent remeshing to improve the mesh quality for the discrete interface. To tackle this problem, Barrett, Garcke, and Nürnberg proposed a novel PFEM (e.g., [8, 7, 10, 9]) which has very good properties with respect to the distribution of mesh points. Precisely, their scheme introduced an implicit tangential motion for mesh points on the moving interface such that these mesh points automatically move tangentially along the interface and maintain good mesh properties, and this scheme has been extended for simulating the grain boundary motion and applications to thermal grooving and sintering [12, 59].

Solid-state dewetting problems belong to the evolution of an open curve/surface governed by surface diffusion and contact line migration [27, 49, 28, 5, 30]. In earlier years, the marker-particle method was first presented for solving sharp-interface

models of solid-state dewetting in two dimensions (2D) [51, 49] and three dimensions (3D) [18]. This method can be thought of as an explicit finite difference scheme; thus it imposes a very severe restriction on the time step for numerical stability. Furthermore, its extension to the 3D case is very tedious, inaccurate, and time-consuming. For isotropic surface diffusion flow of a closed surface, Bänsch, Morin, and Nocetto proposed a PFEM together with a mesh regularization algorithm [3]; Barrett, Garcke, and Nürnberg then developed a simplified and novel variational formulation which leads to good mesh distribution properties and unconditional stability [9, 8]. These stable PFEMs were then generalized to the anisotropic case [6, 11] for a special kind of anisotropy in terms of Riemannian metric form. Other related works for anisotropic flows in the literature can be found in [22, 40, 23] and references therein. Furthermore, PFEMs have also been designed for simulating the evolution of thin solid films on a substrate in the 2D [4, 29] and 3D cases with axisymmetric geometry [58]. But how to design a PFEM for simulating solid-state dewetting problems in the full 3D remains an urgent and challenging problem.

The goal of this paper is to extend our previous works [5, 29] from 2D to 3D by using a variational formulation in terms of the Cahn–Hoffman ξ -vector for simulating solid-state dewetting of thin films. More precisely, the main objectives are as follows: (1) to derive a variational formulation of the sharp-interface model for simulating solid-state dewetting problems in 3D [30]; (2) to develop a PFEM for simulating the solid-state dewetting of thin films in 3D; (3) to demonstrate the capability, efficiency, and accuracy of the proposed PFEM; and (4) to investigate many of the complexities which have been observed in experimental dewetting of patterned islands on substrates, such as Rayleigh instability, pinch-off, edge retraction, and corner mass accumulation.

The rest of the paper is organized as follows. In section 2, we briefly review a sharp-interface model for simulating solid-state dewetting problems in 3D and then present a variational formulation of this sharp-interface model. In section 3, we discretize the variational formulation with a semi-implicit, mixed-form PFEM. In section 4, extensive numerical results are reported to demonstrate the efficiency and accuracy of the PFEM scheme and to show some interesting morphological evolutions of solid-state dewetting in 3D. Finally, some conclusions are drawn in section 5.

2. The model and its variational formulation. In this section, we first review a sharp-interface model obtained recently by the authors [30] for simulating solid-state dewetting of thin films with isotropic/weakly anisotropic surface energies in 3D. Based on this model, we then propose a variational formulation via the Cahn–Hoffman ξ -vector.

2.1. The sharp-interface model. As illustrated in Figure 2.1, we consider that a solid thin film (shaded in blue) lies on a flat, rigid substrate (shaded in gray). (Color available online.) The moving film/vapor interface, labeled as $S := S(t)$, is represented by a time-dependent open surface with a plane curve boundary (i.e., the moving contact line, labeled as $\Gamma := \Gamma(t)$) along the flat substrate S_{sub} (i.e., Oxy -plane). Let U be a time-independent reference domain with $\mathbf{u} = (u_1, u_2)^T \in U \subseteq \mathbb{R}^2$, and assume that the moving surface $S(t) := \mathbf{X}(\mathbf{u}, t)$ (with $\mathbf{X} = (x_1, x_2, x_3)^T$ or $(x, y, z)^T$) can be parameterized as

$$(2.1) \quad \mathbf{X}(\mathbf{u}, t) = (x(\mathbf{u}, t), y(\mathbf{u}, t), z(\mathbf{u}, t))^T : U \times [0, T] \rightarrow \mathbb{R}^3.$$

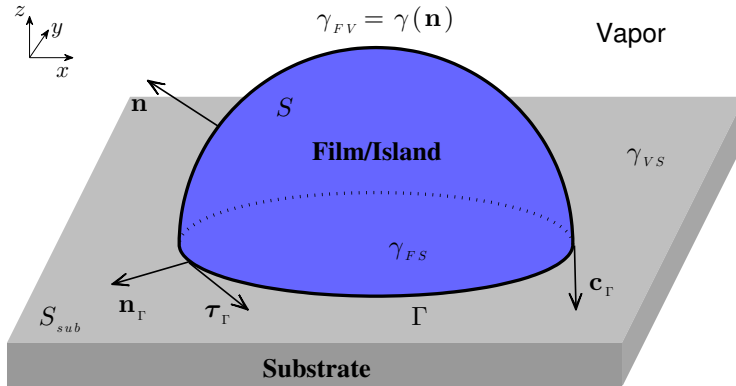


FIG. 2.1. A schematic illustration of solid-state dewetting of thin films on a flat substrate in 3D.

Furthermore, the moving contact line $\Gamma(t) := \mathbf{X}_\Gamma(\cdot, t)$ can be also parameterized over ∂U as

$$(2.2) \quad \mathbf{X}_\Gamma(\cdot, t) = (x_\Gamma(\cdot, t), y_\Gamma(\cdot, t), z_\Gamma(\cdot, t))^T : \partial U \times [0, T] \rightarrow \mathbb{R}^3.$$

By using the approach in [30], we can obtain a sharp-interface model for simulating solid-state dewetting of thin films with isotropic/weakly anisotropic surface energies in 3D as the following dimensionless form:

$$(2.3) \quad \partial_t \mathbf{X} = \Delta_s \mu \mathbf{n}, \quad t > 0,$$

$$(2.4) \quad \mu = \nabla_s \cdot \boldsymbol{\xi}, \quad \boldsymbol{\xi}(\mathbf{n}) = \nabla \hat{\gamma}(\mathbf{p}) \Big|_{\mathbf{p}=\mathbf{n}},$$

where μ is the chemical potential, $\mathbf{n} = (n_1, n_2, n_3)^T$ is the unit outer normal vector of the moving surface S , $\boldsymbol{\xi}(\mathbf{n}) = (\xi_1, \xi_2, \xi_3)^T$ represents the Cahn–Hoffman $\boldsymbol{\xi}$ -vector associated with the surface energy density $\gamma(\mathbf{n})$ (see (1.3)), and $\Delta_s := \nabla_s \cdot \nabla_s$ is the Laplace–Beltrami operator defined on S . The initial condition is given as S_0 with boundary Γ_0 such that

$$(2.5) \quad S_0 := \mathbf{X}(\mathbf{u}, 0) = \mathbf{X}_0(\mathbf{u}) = (x_0(\mathbf{u}), y_0(\mathbf{u}), z_0(\mathbf{u}))^T.$$

The above governing equations are subject to the following boundary conditions:

(i) contact line condition

$$(2.6) \quad z_\Gamma(\cdot, t) = 0, \quad t \geq 0;$$

(ii) relaxed contact angle condition

$$(2.7) \quad \partial_t \mathbf{X}_\Gamma = -\eta(\mathbf{c}_\Gamma^\gamma \cdot \mathbf{n}_\Gamma - \sigma) \mathbf{n}_\Gamma, \quad t \geq 0;$$

(iii) zero-mass flux condition

$$(2.8) \quad (\mathbf{c}_\Gamma \cdot \nabla_s \mu) \Big|_\Gamma = 0, \quad t \geq 0.$$

Here, $0 < \eta < \infty$ represents the contact line mobility, and the vector \mathbf{c}_Γ^γ is defined as a linear combination of \mathbf{c}_Γ and \mathbf{n} ,

$$(2.9) \quad \mathbf{c}_\Gamma^\gamma := (\boldsymbol{\xi} \cdot \mathbf{n}) \mathbf{c}_\Gamma - (\boldsymbol{\xi} \cdot \mathbf{c}_\Gamma) \mathbf{n},$$

where $\mathbf{c}_\Gamma = (c_{\Gamma,1}, c_{\Gamma,2}, c_{\Gamma,3})^T$ is called the unit conormal vector, which is normal to Γ , is tangent to the surface S , and points outwards, $\mathbf{n}_\Gamma = (n_{\Gamma,1}, n_{\Gamma,2}, 0)^T$ is the unit outer normal vector of Γ on the substrate (as shown in Figure 2.1), and $\sigma := (\gamma_{VS} - \gamma_{FS})/\gamma_0$ is a (dimensionless) material constant with γ_0 being the characteristic unit for surface energy, where the two constants γ_{VS} and γ_{FS} represent the vapor/substrate and film/substrate surface energy densities, respectively.

Condition (i) (i.e., (2.6)) ensures that the contact line moves along the substrate during time evolution. Condition (ii) prescribes a contact angle condition along the moving contact line. In order to understand this condition, we may consider two limiting cases $\eta = 0$ and $\eta = \infty$: (1) when $\eta = 0$, the contact line moving velocity is zero, and we prescribe a fixed boundary condition such that the contact line does not move; and (2) when $\eta \rightarrow \infty$, as we always assume that the moving velocity should be finite, condition (ii) will reduce to the so-called anisotropic Young equation [30, 4]

$$(2.10) \quad \mathbf{c}_\Gamma^\gamma \cdot \mathbf{n}_\Gamma - \sigma = 0,$$

which prescribes an equilibrium contact angle condition. Therefore, condition (ii) actually allows a relaxation process for the dynamic contact angle evolving to its equilibrium contact angle [49, 28]. Condition (iii) ensures that the total volume/mass of the thin film is conserved during the evolution, i.e., zero-mass flux at the moving contact line. We remark that if the moving surface has more than one closed curve as its boundary (see examples in Figure 4.10), then the boundary conditions (2.6)–(2.8) should be satisfied on each boundary curve.

The above sharp-interface model (2.3)–(2.4) with boundary conditions (2.6)–(2.8) are derived based on the consideration of thermodynamic variation [4, 30], and therefore it naturally satisfies the thermodynamic-consistent physical law. More precisely, the total (dimensionless) free energy of the system, including the interface energy W_{int} and substrate energy W_{sub} , can be written as [4, 30]

$$(2.11) \quad W(t) := W_{\text{int}} + W_{\text{sub}} = \int_{S(t)} \gamma(\mathbf{n}) dS - \sigma A(\Gamma),$$

where $A(\Gamma)$ denotes the surface area enclosed by the contact line curve Γ on the substrate. It can be easily shown that during the evolution which is governed by the above sharp-interface model [30], the total volume of the thin film is conserved and the total free energy satisfies the following dissipation law:

$$(2.12) \quad \frac{d}{dt} W(t) = - \int_{S(t)} |\nabla_S \mu|^2 dS - \eta \int_{\Gamma(t)} \left(\mathbf{c}_\Gamma^\gamma \cdot \mathbf{n}_\Gamma - \sigma \right)^2 d\Gamma \leq 0, \quad t \geq 0.$$

2.2. The variational formulation. Let $S := S(t) \in C^2(U)$ be a smooth surface with smooth boundary $\Gamma := \Gamma(t)$, and assume that $f \in C(\bar{S})$. Denote the surface gradient operator as $\nabla_S := (\underline{D}_1, \underline{D}_2, \underline{D}_3)^T$; then the integration by parts on an open smooth surface S with smooth boundary Γ can be written as [30, 20]

$$(2.13) \quad \int_S \underline{D}_i f dS = \int_S f \mathcal{H} n_i dS + \int_\Gamma f c_{\Gamma,i} d\Gamma,$$

where $\mathcal{H} = \nabla_s \cdot \mathbf{n}$ is the mean curvature of the surface S and $\mathbf{c}_\Gamma = (c_{\Gamma,1}, c_{\Gamma,2}, c_{\Gamma,3})^T$ is the conormal vector defined above. Following the above formula, we can naturally define the derivative $\nabla_s f$ in the weak sense. Then, we can define the functional space $L^2(S)$ as

$$(2.14) \quad L^2(S) := \left\{ f : S \rightarrow \mathbb{R}, \text{ and } \|f\|_{L^2(S)} = \left(\int_S f^2 dS \right)^{\frac{1}{2}} < +\infty \right\},$$

equipped with the L^2 inner product for any scalar- or vector-valued functions f_1, f_2 defined over the surface S as follows:

$$(2.15) \quad \langle f_1, f_2 \rangle_S := \int_S f_1 \cdot f_2 dS.$$

The Sobolev space $H^1(S)$ can be naturally defined as

$$(2.16) \quad H^1(S) := \left\{ f : S \rightarrow \mathbb{R}, f \in L^2(S), \underline{D}_i f \in L^2(S) \quad \forall 1 \leq i \leq 3 \right\},$$

equipped with the norm $\|f\|_{H^1(S)} := (\|f\|_{L^2(S)}^2 + \|\nabla_s f\|_{L^2(S)}^2)^{\frac{1}{2}}$. Furthermore, if we denote $T_s : H^1(S) \rightarrow L^2(\Gamma)$ as the trace operator, we can define the following functional space with the homogeneous Dirichlet boundary condition:

$$(2.17) \quad H_0^1(S) := \left\{ f : f \in H^1(S), T_s f = 0 \right\}.$$

Then, we can define a subset of the functional space $H^1(U)$ which is used for the solid-state dewetting problem

$$(2.18) \quad H_\alpha^1(U) := \left\{ \varphi \in H^1(U), \varphi \Big|_{\partial U} = \alpha \right\},$$

where the function $\alpha \in L^2(\partial U)$ is given. We note that $H_0^1(U)$ denotes the functions in $H^1(U)$ with traces being zeros.

We now propose the following variational formulation for the sharp-interface model (2.3)–(2.4) with the boundary conditions (2.6)–(2.8): given the initial surface $S_0 := \mathbf{X}_0(U)$ with its boundary Γ_0 defined in (2.5), find its evolution surfaces $S(t) := \mathbf{X}(U, t) \in H_\alpha^1(U) \times H_\beta^1(U) \times H_0^1(U)$ and the chemical potential $\mu(\cdot, t) \in H^1(S)$ such that

$$(2.19a) \quad \langle \partial_t \mathbf{X} \cdot \mathbf{n}, \varphi \rangle_S + \langle \nabla_s \mu, \nabla_s \varphi \rangle_S = 0 \quad \forall \varphi \in H^1(S),$$

$$(2.19b) \quad \begin{aligned} \langle \mu, \mathbf{n} \cdot \boldsymbol{\omega} \rangle_S - \sum_{k=1}^3 \langle \gamma(\mathbf{n}) \nabla_s x_k, \nabla_s \omega_k \rangle_S \\ + \sum_{k,l=1}^3 \langle \xi_k \nabla_s x_k, n_l \nabla_s \omega_l \rangle_S = 0 \quad \forall \boldsymbol{\omega} \in [H_0^1(S)]^3, \end{aligned}$$

where α, β represent the x -, y -coordinates of the moving contact line at time t , i.e., $\alpha = x_\Gamma(\cdot, t)$, $\beta = y_\Gamma(\cdot, t)$, and $\boldsymbol{\xi}(\mathbf{n}) = (\xi_1, \xi_2, \xi_3)^T$ represents the Cahn–Hoffman $\boldsymbol{\xi}$ -vector associated with the surface energy density $\gamma(\mathbf{n})$ (see the definition in (1.3)). Here, $\Gamma(t) := \mathbf{X}_\Gamma(\cdot, t) = (x_\Gamma(\cdot, t), y_\Gamma(\cdot, t), 0)^T$ is jointly determined by the relaxed angle boundary condition (2.7) in the above weak formulation.

In the above weak formulation, (2.19a) can be obtained by reformulating (2.3) as $\partial_t \mathbf{X} \cdot \mathbf{n} = \Delta_S \mu$, multiplying a scalar test function $\varphi \in H^1(S)$, integrating over $S(t)$, integrating by parts, and noting the zero-mass flux boundary condition (2.8). Similarly, by multiplying n_l and (2.4), we obtain the following equation [16]:

$$(2.20) \quad \mu n_l = (\nabla_S \cdot \boldsymbol{\xi}) n_l = \underline{D}_k(\xi_k n_l) - \underline{D}_k(\gamma(\mathbf{n}) \underline{D}_k x_l) - \gamma(\mathbf{n}) \mathcal{H} n_l, \quad l = 1, 2, 3,$$

where summation over k is from 1 to 3. By multiplying (2.20) with ω_l on both sides, summing over $l = 1, 2, 3$, integrating over S , and integrating by parts, we can obtain (2.19b). For more details, please refer to [16]. We note that (2.19b) has also been used in some works related to anisotropic geometric evolution equations [16, 22, 11, 40].

In the isotropic case, i.e., $\gamma(\mathbf{n}) \equiv 1$, we have $\boldsymbol{\xi}(\mathbf{n}) = \mathbf{n}$. By using the fact that $\underline{D}_k x_l = \delta_{kl} - n_k n_l$, we can obtain $\sum_{k,l=1}^3 \langle n_k \nabla_S x_k, n_l \nabla_S \omega_l \rangle_S = 0$. Therefore, (2.19b) will reduce to the variational formulation of the curvature term related to the Laplace–Beltrami operator [3, 9]

$$(2.21) \quad \langle \mu, \mathbf{n} \cdot \boldsymbol{\omega} \rangle_S - \sum_{k=1}^3 \langle \nabla_S x_k, \nabla_S \omega_k \rangle_S = 0 \quad \forall \boldsymbol{\omega} \in (H_0^1(S))^3.$$

In general, it is not easy to obtain the energy stability based on the discretization of the variational formulation defined in (2.19a)–(2.19b). Specifically, in the isotropic case, the stability bound for the discretization of (2.21) has been established for the evolution of a closed surface [3, 9]. Based on our numerical experiments, the variational formulation defined in (2.19a)–(2.19b) and its PFEM perform very well in terms of stability, efficiency, and accuracy in practical computations.

3. The parametric finite element approximation. In this section, based on the variational formulation (2.19a)–(2.19b), we discretize the problem via a semi-implicit PFEM and prove the well-posedness of the discrete scheme.

To present the PFEM for the variational problem, we first take the discrete time as $0 = t_0 < t_1 < t_2 < \dots < t_M$ and denote time steps as $\tau_m = t_{m+1} - t_m$ for $0 \leq m \leq M-1$. In the spatial level, we assume that the evolution surfaces $\{S(t_m)\}_{m=0}^M$ are discretized by polygonal surfaces $\{S^m\}_{m=0}^M$ such that

$$(3.1) \quad S^m = \bigcup_{j=1}^N \bar{D}_j^m, \quad \text{where } \{\bar{D}_j^m\}_{j=1}^N \text{ are mutually disjoint triangles.}$$

Here, we assume that the discrete surface S^m has K different vertices (labeled as $\{\mathbf{q}_k^m\}_{k=1}^K$), and the boundary of S^m is a closed polygonal curve $\Gamma^m = \bigcup_{j=1}^{N_c} \bar{h}_j^m$, where $\{\bar{h}_j^m\}_{j=1}^{N_c}$ are a sequence of connected line segments that is positively oriented; i.e., if you walk along the direction of the oriented boundary, the surface is at your left side. Moreover, we have the following assumption about the polygonal surface at each time step:

$$(3.2) \quad |\bar{D}_j^m| > 0, \quad 1 \leq j \leq N, \quad 0 \leq m \leq M,$$

which ensures that vertices of polygonal surface will not merge during the evolution.

We can define the following finite dimensional spaces over Γ^m and S^m :

$$(3.3a) \quad V^h(\Gamma^m) := \left\{ \varphi \in C(\Gamma^m, \mathbb{R}) : \varphi \Big|_{\bar{h}_j^m} \in \mathbf{P}_1 \ \forall 1 \leq j \leq N_c \right\} \subset H^1(\Gamma^m),$$

$$(3.3b) \quad V^h(S^m) := \left\{ \varphi \in C(S^m, \mathbb{R}) : \varphi \Big|_{\bar{D}_j^m} \in \mathbf{P}_1 \ \forall 1 \leq j \leq N \right\} \subset H^1(S^m),$$

where \mathbf{P}_1 denotes all polynomials with degree at most 1, which yields piecewise linear functions on each element. If $\alpha \in V^h(\Gamma^m)$, we can define a subset of the space $V^h(S^m)$ on S^m with boundary value given by a function α as

$$(3.4) \quad \mathcal{V}_\alpha^h(S^m) := \left\{ \varphi \in V^h(S^m) : \varphi \Big|_{\Gamma^m} = \alpha \right\}.$$

Again, for simplicity of notation, we denote \mathcal{V}_0^h as the space $V^h(S^m)$ with zero values on the boundary Γ^m .

Now, we can define the following mass-lumped inner product to approximate the integration on S^m :

$$(3.5) \quad \langle f_1, f_2 \rangle_m^h = \frac{1}{3} \sum_{j=1}^N |D_j^m| \sum_{k=1}^3 f_1 \left((\mathbf{q}_{j_k}^m)^- \right) \cdot f_2 \left((\mathbf{q}_{j_k}^m)^- \right),$$

where $|D_j^m|$ is the area of the triangle D_j^m , and f_1, f_2 are two scalar or vector functions defined on S^m with possible jumps across each edge of the triangle in 3D. We define the one-sided limit $f_1((\mathbf{q}_{j_k}^m)^-)$ as the limit of $f_1(\mathbf{x})$ when \mathbf{x} approaches $\mathbf{q}_{j_k}^m$ from the triangle surface D_j^m , i.e., $f_1((\mathbf{q}_{j_k}^m)^-) = \lim_{D_j^m \ni \mathbf{x} \rightarrow \mathbf{q}_{j_k}^m} f_1(\mathbf{x})$.

We assume that $\{\mathbf{q}_{j_1}^m, \mathbf{q}_{j_2}^m, \mathbf{q}_{j_3}^m\}$ are the three vertices of the triangle surface D_j^m and are ordered in the anticlockwise direction when viewing from top to bottom. It should be noted that the normal vector $\mathbf{n}^m = (n_1^m, n_2^m, n_3^m)^T$ of the surface S^m is a step function with discontinuities across the edges of each triangle surface. Let \mathbf{n}_j^m be the unit normal vector on D_j^m ; we can numerically evaluate it as

$$(3.6) \quad \mathbf{n}_j^m := \mathbf{n}^m \Big|_{D_j^m} = \frac{(\mathbf{q}_{j_2}^m - \mathbf{q}_{j_1}^m) \times (\mathbf{q}_{j_3}^m - \mathbf{q}_{j_1}^m)}{|(\mathbf{q}_{j_2}^m - \mathbf{q}_{j_1}^m) \times (\mathbf{q}_{j_3}^m - \mathbf{q}_{j_1}^m)|} \quad \forall 1 \leq j \leq N.$$

For the discrete boundary curve Γ^m , it is a closed plane curve and consists of a sequence of connected line segments on the substrate (*Oxy*-plane). We assume that $\{\mathbf{p}_{j_1}^m, \mathbf{p}_{j_2}^m\}$ are the two vertices of a line segment h_j^m which are ordered according to the orientation of the curve. Let \mathbf{n}_r^m denote the unit normal vector of the boundary curve Γ^m along the substrate; then \mathbf{n}_r^m is also a step function with discontinuities across the vertices of each line segment. Let $\mathbf{n}_{\Gamma,j}^m$ represent the unit normal vector of Γ^m on the line segment h_j^m ; then

$$(3.7) \quad \mathbf{n}_{\Gamma,j}^m = \mathbf{n}_r^m \Big|_{h_j^m} = \frac{(\mathbf{p}_{j_2}^m - \mathbf{p}_{j_1}^m) \times \mathbf{e}_3}{|(\mathbf{p}_{j_2}^m - \mathbf{p}_{j_1}^m) \times \mathbf{e}_3|} \quad \forall 1 \leq j \leq N_c,$$

where the unit vector $\mathbf{e}_3 = (0, 0, 1)^T$. Similarly, \mathbf{c}_r^m is the unit conormal vector defined on the polygonal curve Γ^m along the substrate, and it is also a step function which can be numerically evaluated as

$$(3.8) \quad \mathbf{c}_{\Gamma,j}^m = \mathbf{c}_r^m \Big|_{h_j^m} = \frac{(\mathbf{p}_{j_2}^m - \mathbf{p}_{j_1}^m) \times \mathbf{n}_{k_j}^m}{|(\mathbf{p}_{j_2}^m - \mathbf{p}_{j_1}^m) \times \mathbf{n}_{k_j}^m|} \quad \forall 1 \leq j \leq N_c,$$

where $\mathbf{n}_{k_j}^m$ is the unit outer normal vector of the triangle surface $D_{k_j}^m$ which contains the line segment h_j^m (as shown in Figure 3.1(b)).

Let $S^m := \mathbf{X}^m(U)$ and $\Gamma^m := \mathbf{X}_r^m(\partial U) = (x_r^m, y_r^m, 0)^T$ be the numerical approximations of the moving surface $S(t_m) := \mathbf{X}(U, t_m)$ and its boundary line

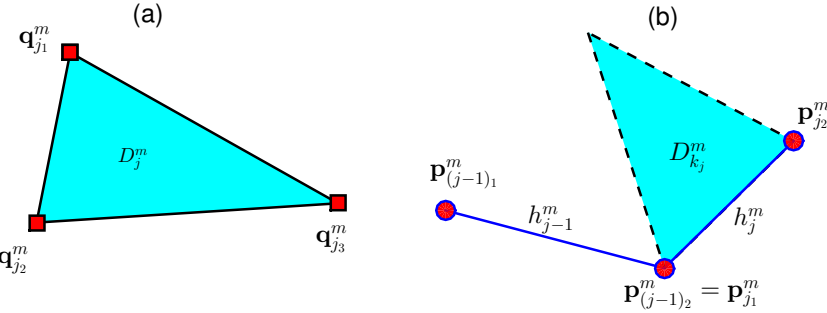


FIG. 3.1. A schematic illustration of surface triangle mesh when viewing from top to bottom: (a) A triangle mesh with no edges on the boundary; (b) a triangle mesh with an edge (shown in blue) on the boundary. (Color available online.)

$\Gamma(t_m) := \mathbf{X}_\Gamma(\partial U, t_m)$, respectively. Take $S^0 = \mathbf{X}^0(U)$ with $\alpha_0, \beta_0 \in V^h(\Gamma^0)$ as the numerical approximations of $x_\Gamma(\cdot, 0), y_\Gamma(\cdot, 0)$, respectively.

Then, a semi-implicit PFEM for the variational problem (2.19a)–(2.19b) can be stated as: given $S^0 = \bigcup_{j=1}^N \bar{D}_j^0$ which is an initial polygonal surface and its boundary curve $\Gamma^0 = \bigcup_{j=1}^{N_c} \bar{h}_j^0$, for $m \geq 0$, find a sequence of polygonal surfaces $S^{m+1} := \mathbf{X}^{m+1}(U) \in \mathcal{V}_\alpha^h(S^m) \times \mathcal{V}_\beta^h(S^m) \times \mathcal{V}_0^h(S^m)$ and chemical potentials $\mu^{m+1} \in V^h(S^m)$ such that

(3.9a)

$$\left\langle \frac{\mathbf{X}^{m+1} - \mathbf{X}^m}{\tau_m}, \varphi_h \mathbf{n}^m \right\rangle_m^h + \left\langle \nabla_s \mu^{m+1}, \nabla_s \varphi_h \right\rangle_m^h = 0 \quad \forall \varphi_h \in V^h(S^m),$$

(3.9b)

$$\left\langle \mu^{m+1}, \mathbf{n}^m \cdot \boldsymbol{\omega}_h \right\rangle_m^h - \sum_{l=1}^3 \left\langle \gamma^m \nabla_s x_l^{m+1}, \nabla_s \omega_{h,l} \right\rangle_m^h = \mathcal{G}^m(\boldsymbol{\omega}_h) \quad \forall \boldsymbol{\omega}_h \in [\mathcal{V}_0^h(S^m)]^3,$$

where γ^m and \mathcal{G}^m are explicitly calculated as

$$(3.10) \quad \gamma^m = \gamma(\mathbf{n}^m), \quad \mathcal{G}^m(\boldsymbol{\omega}_h) = - \sum_{k,l=1}^3 \left\langle \xi_k^m \nabla_s x_k^m, n_l^m \nabla_s \omega_{h,l} \right\rangle_m^h,$$

with $\boldsymbol{\xi}^m = \boldsymbol{\xi}(\mathbf{n}^m) = (\xi_1^m, \xi_2^m, \xi_3^m)^T$, $\boldsymbol{\omega}_h = (\omega_{h,1}, \omega_{h,2}, \omega_{h,3})^T$, and α, β are the x -, y -coordinates of the contact line Γ^{m+1} , i.e., $\alpha := x_\Gamma^{m+1}, \beta := y_\Gamma^{m+1}$.

We note here that the boundary curve Γ^{m+1} is first updated from Γ^m by explicitly solving the relaxed contact angle condition defined in (2.7), and then by using Γ^{m+1} as the Dirichlet boundary condition, we solve the above PFEM to obtain the new polygonal surface S^{m+1} . More precisely, the algorithm for updating Γ^{m+1} can be described as follows (shown in Figure 3.2):

- Calculate $\mathbf{n}_{k_j}^m, \mathbf{n}_{\Gamma,j}^m$, and $\mathbf{c}_{\Gamma,j}^m$ via (3.6), (3.7), and (3.8), and then, by using forward Euler scheme to approximate the relaxed contact angle condition, we can obtain λ_j^m and \mathbf{V}_j^m for each line segment h_j^m as

$$\lambda_j^m := -\tau_m \eta (\mathbf{c}_{\Gamma,j}^{\gamma,m} \cdot \mathbf{n}_{\Gamma,j}^m - \sigma), \quad \mathbf{V}_j^m := \lambda_j^m \mathbf{n}_{\Gamma,j}^m, \quad 1 \leq j \leq N_c,$$

where $\mathbf{c}_{\Gamma,j}^{\gamma,m} := (\boldsymbol{\xi}(\mathbf{n}_{k_j}^m) \cdot \mathbf{n}_{k_j}^m) \mathbf{c}_{\Gamma,j}^m - (\boldsymbol{\xi}(\mathbf{n}_{k_j}^m) \cdot \mathbf{c}_{\Gamma,j}^m) \mathbf{n}_{k_j}^m$.

- If $\mathbf{n}_{\Gamma,j-1}^m \parallel \mathbf{n}_{\Gamma,j}^m$, we update the segmentation point $\mathbf{p}_{j_1}^m$ by moving along the displacement vector $\frac{1}{2}(\mathbf{V}_{j-1}^m + \mathbf{V}_j^m)$.
- If $\mathbf{n}_{\Gamma,j-1}^m \nparallel \mathbf{n}_{\Gamma,j}^m$, we first move each line segment h_j^m along its normal direction by an increment vector $\mathbf{V}_j^m = \lambda_j^m \mathbf{n}_{\Gamma,j}^m$, then calculate the intersection point of the updated adjacent edges, and take it as the new segmentation point.

In summary, the new segmentation point $\mathbf{p}_{j_1}^{m+1}$ can be updated as the following formula:

$$(3.11) \quad \mathbf{p}_{j_1}^{m+1} = \begin{cases} \mathbf{p}_{j_1}^m + \frac{1}{2}(\mathbf{V}_{j-1}^m + \mathbf{V}_j^m) & \text{if } \mathbf{n}_{\Gamma,j-1}^m \parallel \mathbf{n}_{\Gamma,j}^m, \\ \mathbf{p}_{j_1}^m + \frac{\lambda_{j-1}^m - \lambda_j^m R_j^m}{1 - |R_j^m|^2} \mathbf{n}_{\Gamma,j-1}^m + \frac{\lambda_j^m - \lambda_{j-1}^m R_j^m}{1 - |R_j^m|^2} \mathbf{n}_{\Gamma,j}^m & \text{if } \mathbf{n}_{\Gamma,j-1}^m \nparallel \mathbf{n}_{\Gamma,j}^m, \end{cases}$$

where $R_j^m = \mathbf{n}_{\Gamma,j-1}^m \cdot \mathbf{n}_{\Gamma,j}^m$. By making use of

$$(3.12) \quad (\mathbf{p}_{j_1}^{m+1} - \mathbf{p}_{j_1}^m) \cdot \mathbf{n}_{\Gamma,j-1}^m = \lambda_{j-1}^m, \quad (\mathbf{p}_{j_1}^{m+1} - \mathbf{p}_{j_1}^m) \cdot \mathbf{n}_{\Gamma,j}^m = \lambda_j^m,$$

it is easy to obtain the above formula.

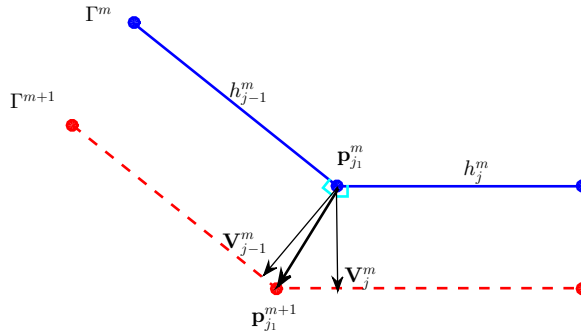


FIG. 3.2. The boundary curve is determined by a polygonal line, which can be updated in the following two steps: (1) Shift each line segment h_j^m of the curve Γ^m along its normal direction by a displacement vector $\mathbf{V}_j^m = \lambda_j^m \mathbf{n}_{\Gamma,j}^m$ via the relaxed contact angle condition; (2) calculate the intersection point of the updated adjacent edges, and take it as the segmentation point of the polygonal line Γ^{m+1} . In particular, if $\mathbf{n}_{\Gamma,j-1}^m \parallel \mathbf{n}_{\Gamma,j}^m$, we move the point $\mathbf{p}_{j_1}^m$ by a displacement vector $\frac{1}{2}(\mathbf{V}_{j-1}^m + \mathbf{V}_j^m)$.

We remark that the above discrete problem results in a linear algebra system which can be efficiently solved via the sparse LU decomposition or GMRES method. Moreover, we have the following theorem for the well-posedness of the proposed discrete scheme.

THEOREM 3.1 (well-posedness of the PFEM). *The above discrete variational problem (3.9a)–(3.9b) admits a unique solution (i.e., it is well-posed).*

Proof. To prove the well-posedness of the PFEM scheme, we need to prove that the linear system obtained from (3.9a)–(3.9b) has a unique solution. By noting that the moving contact line Γ^{m+1} is first updated via the relaxed angle boundary condition in the above PFEM, we can regard it as a Dirichlet-type boundary condition for the variational problem (3.9a)–(3.9b). It is equivalent to proving that the corresponding homogeneous linear system has only the zero solution.

Therefore, the well-posedness of the discrete problem (3.9a)–(3.9b) is equivalent to that of the following homogeneous linear system: find $\{\mathbf{X}^{m+1}, \mu^{m+1}\} \in \{[\mathcal{V}_0^h(S^m)]^3, V^h(S^m)\}$ such that

$$(3.13a) \quad \langle \mathbf{X}^{m+1} \cdot \mathbf{n}^m, \varphi_h \rangle_m^h + \tau_m \langle \nabla_s \mu^{m+1}, \nabla_s \varphi_h \rangle_m^h = 0 \quad \forall \varphi_h \in V^h(S^m),$$

$$(3.13b) \quad \langle \mu^{m+1}, \mathbf{n}^m \cdot \boldsymbol{\omega}_h \rangle_m^h - \langle \gamma(\mathbf{n}^m) \nabla_s \mathbf{X}^{m+1}, \nabla_s \boldsymbol{\omega}_h \rangle_m^h = 0 \quad \forall \boldsymbol{\omega}_h \in (\mathcal{V}_0^h(S^m))^3.$$

By choosing the test functions as $\varphi_h = \mu^{m+1}, \boldsymbol{\omega}_h = \mathbf{X}^{m+1}$, we can immediately obtain

$$(3.14) \quad \tau_m \langle \nabla_s \mu^{m+1}, \nabla_s \mu^{m+1} \rangle_m^h + \langle \gamma(\mathbf{n}^m) \nabla_s \mathbf{X}^{m+1}, \nabla_s \mathbf{X}^{m+1} \rangle_m^h = 0.$$

By noting that $\gamma(\mathbf{n}^m) > 0$ for all $\mathbf{n}^m \in S^2$, we obtain directly $\mathbf{X}^{m+1} = \mathbf{0}$ by using the zero boundary condition, and, moreover, we have $\mu \equiv \mu^c$ (i.e., a constant). Furthermore, by substituting $\mathbf{X}^{m+1} = 0$ into (3.13b), we have

$$(3.15) \quad \mu^c \langle \mathbf{n}^m, \boldsymbol{\omega}^h \rangle_m^h = 0.$$

By choosing $\boldsymbol{\omega}^h = \mathbf{g}_j^m \phi_j^m$ with the weighted normal vector \mathbf{g}_j^m defined as

$$(3.16) \quad \mathbf{g}_j^m := \frac{\sum_{D_k^m \in \mathcal{T}_j^m} |D_k^m| \mathbf{n}_k^m}{\sum_{D_k^m \in \mathcal{T}_j^m} |D_k^m|}, \quad \text{with } \mathcal{T}_j^m := \{D_k^m : \mathbf{q}_j^m \in \bar{D}_k^m\},$$

and $\phi_j^m \in V^h(S^m)$ being the nodal basic function at point \mathbf{q}_j^m , it immediately yields $\mu^c = 0$ by noting the assumption (3.2) and (3.5).

Therefore, the corresponding homogeneous linear system only has the zero solution, which indicates the existence and uniqueness of solution for our PFEM. \square

The above-proposed PFEM via the ξ -vector formulation is an extension to the 3D case based on our previous works in 2D [29]. The idea behind the variational formulation is using the decomposition of the Cahn–Hoffman ξ -vector into the normal and tangential components [29]. In the discrete scheme, the normal component is discretized implicitly, while the tangential components are explicitly discretized. During the practical computation, we need to redistribute mesh points uniformly in 2D according to the arc-length for the polygonal boundary line in each time step; similarly, we also use the mesh redistribution algorithm discussed in [3] to prevent the mesh distortion for the triangular surface mesh.

Furthermore, in the PFEM, since $S^{m+1} := \mathbf{X}^{m+1}(S^m)$ is assumed to be parameterized over S^m , the operator ∇_s can then be very easily numerically calculated. More precisely, consider the triangular surface D_j^m with vertices $\{\mathbf{q}_{j_1}^m, \mathbf{q}_{j_2}^m, \mathbf{q}_{j_3}^m\}$ ordered in the anticlockwise direction; we then have

$$(3.17) \quad \nabla_s B_{j_1}(S^m) \Big|_{D_j^m} = \frac{(\mathbf{q}_{j_3}^m - \mathbf{q}_{j_2}^m) \times \mathbf{n}_j^m}{2|D_j^m|},$$

where $B_{j_1} \in V^h(S^m)$ is the nodal basis function defined at point $\mathbf{q}_{j_1}^m$. Similarly, we can easily obtain $\nabla_s B_{j_2}$ and $\nabla_s B_{j_3}$. Therefore, for any piecewise linear function $\phi \in V^h(S^m)$, we can have

$$(3.18) \quad \nabla_s \phi \Big|_{D_j^m} = \sum_{i=1}^3 \phi(\mathbf{q}_{j_i}^m) \nabla_s B_{j_i}.$$

4. Numerical results. In this section, we implement the proposed PFEM, show some equilibrium convergence results, and perform many numerical simulations to demonstrate the efficiency and accuracy of the proposed scheme. In the following simulations, we use the uniform time step, i.e., $\tau = \tau_m$, $m = 0, 1, 2, \dots$.

4.1. Equilibrium convergence. The mathematical description of the equilibrium shape has been investigated in [30]. Here, we present some numerical equilibrium convergence results by solving the kinetic sharp-interface model via the proposed PFEM scheme.

From the relaxed contact angle boundary condition (2.7), we know that the contact line mobility η precisely controls the relaxation rate of the contact angle towards its equilibrium state. The large η will accelerate the relaxation process [49, 27, 26]. Here, we numerically investigate the effect of η on the evolution of the dynamic contact angles. We numerically define the following average contact angle $\bar{\theta}^m$ as the indicator:

$$(4.1) \quad \bar{\theta}^m = \frac{1}{N_c} \sum_{j=1}^{N_c} \arccos(\mathbf{c}_{\Gamma,j}^m \cdot \mathbf{n}_{\Gamma,j}^m),$$

where $\mathbf{n}_{\Gamma,j}^m$ and $\mathbf{c}_{\Gamma,j}^m$ are the unit normal and conormal vectors defined on the j th line segment h_j^m of the boundary curve Γ^m .

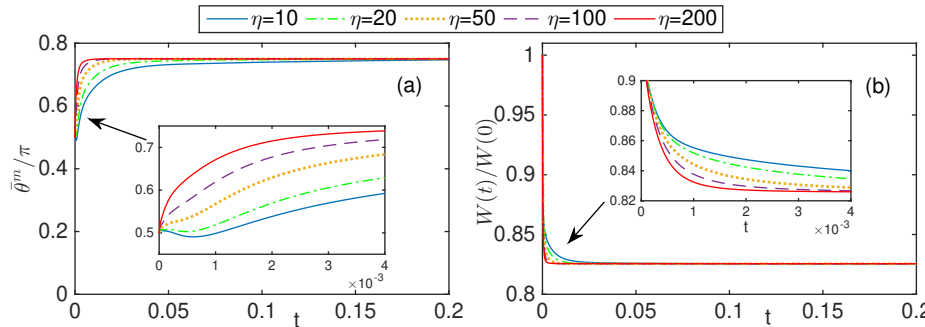


FIG. 4.1. (a) The temporal evolution of the average contact angle $\bar{\theta}^m$ defined in (4.1); (b) the temporal evolution of the normalized energy $W(t)/W(0)$ for different choices of mobility, where the initial shape of the island film with isotropic surface energy is chosen as a unit cube, and the computational parameters are chosen as $\sigma = \cos(3\pi/4)$.

Figure 4.1 shows the temporal evolution of $\bar{\theta}^m$ and the normalized energy $W(t)/W(0)$ under different choices of the contact line mobility η . The initial shape of the island film is chosen as a unit cube, and $\sigma = \cos(3\pi/4)$. From the figure, we can observe that the larger mobility η will accelerate the process of relaxation such that the contact angles evolve faster towards its equilibrium contact angle $3\pi/4$. As shown in Figure 4.1, the energy decays faster for larger mobility but finally converges to the same equilibrium state. It indicates that the equilibrium contact angle, as well as the equilibrium shape, is independent of the choice of the contact line mobility η . Meanwhile, the total volume loss (not shown here) of the island film is always below 0.5% during the numerical simulations. In the following numerical simulations, the contact line mobility is chosen to be very large (e.g., $\eta = 100$). This choice of η will result in a very quick convergence to the equilibrium contact angle (defined in (2.10)). The

detailed investigation of the influence of the parameter η on the solid-state dewetting evolution process and equilibrium shapes was performed in 2D [49].

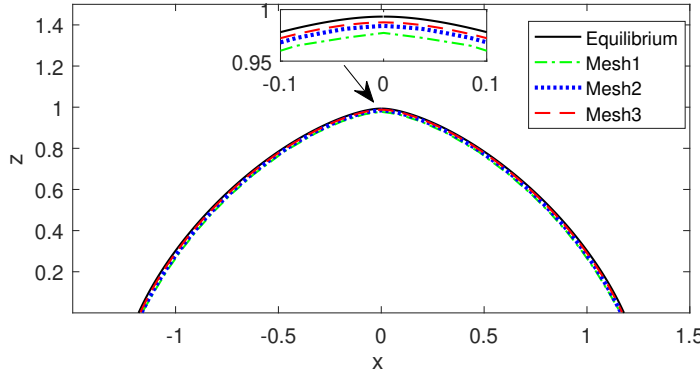


FIG. 4.2. Comparisons of the cross-section profiles along the x -direction of the numerical equilibrium shapes under different meshes with its theoretical equilibrium shape, where the initial shape is chosen as a $(1, 2, 1)$ cuboid, the surface energy $\gamma(\mathbf{n}) = 1 + 0.25(n_1^4 + n_2^4 + n_3^4)$, and $\sigma = \cos(15\pi/36)$. The theoretical equilibrium shape (black line) is constructed by the Winterbottom construction [50, 4].

We next show a convergence result between the numerical equilibrium shapes by solving the proposed sharp-interface model and its theoretical equilibrium shape. Figure 4.2 depicts equilibrium shapes under different mesh sizes, where $\sigma = \cos(15\pi/36)$, $\gamma(\mathbf{n}) = 1 + 0.25(n_1^4 + n_2^4 + n_3^4)$. The initial shape is chosen as a $(1, 2, 1)$ cuboid; then we numerically evolve it until the equilibrium state by using different meshes, which are given by a set of small isosceles right triangles. If we define the mesh size indicator h as the length of the hypotenuse of the isosceles right triangle, then “Mesh 1” represents the initial mesh with $h = h_0 = 0.125$, and the time step is chosen as $\tau = \tau_0 = 0.00125$ for numerical computation. Meanwhile, the time steps for “Mesh 2” ($h = h_0/2$) and “Mesh 3” ($h = h_0/4$) are chosen as $\tau = \tau_0/4$ and $\tau = \tau_0/16$, respectively. For a better comparison, we plot the cross-section profiles along the x -direction for the numerical equilibrium shapes and the theoretical equilibrium shape. As shown in Figure 4.2, we can clearly observe that as the computational mesh size gradually decreases, the numerical equilibrium shapes uniformly converge to the theoretical equilibrium shape.

4.2. For the isotropic case. We first focus on the isotropic surface energy case, i.e., $\gamma(\mathbf{n}) \equiv 1$. We start with a numerical example by initially choosing a small cuboid island with $(1, 4, 1)$ representing its width, length, and height, and the material constant is chosen as $\sigma = \cos(3\pi/4)$. The cuboid is initially almost uniformly discretized into 3584 small isosceles right triangles with a total of 1833 vertices and 80 vertices on the boundary curve. The time step is chosen uniformly as $\tau = 2 \times 10^{-4}$. As is shown in Figure 4.3, it depicts several snapshots of the triangular surface mesh of the island towards its equilibrium shape. We can clearly observe that the sharp corner of the island gradually disappears and becomes smoother and smoother, and finally, the island evolves into a perfect spherical shape which is truncated by the flat substrate.

In general, a short island film tends to form a single spherical shape in order to arrive at its lowest energy state, while a long island film will pinch off and agglomerate into pieces of small isolated islands before it reaches a single spherical shape. This

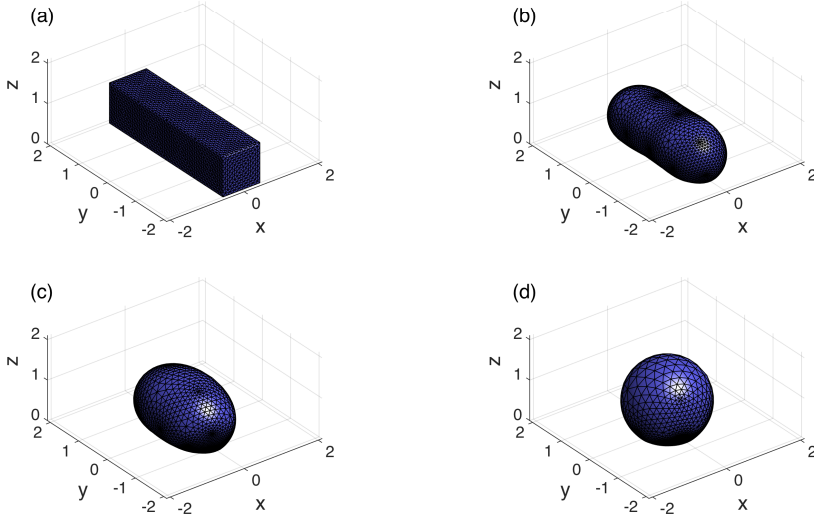


FIG. 4.3. Several snapshots in the evolution of an initial $(1, 4, 1)$ cuboid island towards its equilibrium shape: (a) $t = 0$; (b) $t = 0.10$; (c) $t = 0.20$; (d) $t = 1.94$, where the material constant is chosen as $\sigma = \cos(3\pi/4)$.

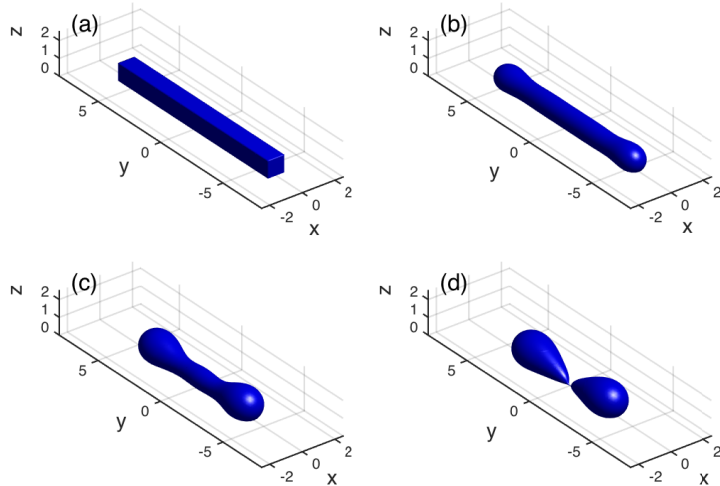


FIG. 4.4. Several snapshots in the evolution of an initial $(1, 12, 1)$ cuboid island until its pinch-off: (a) $t = 0$; (b) $t = 0.01$; (c) $t = 0.75$; (d) $t = 1.07$, where the material constant is chosen as $\sigma = \cos(3\pi/4)$. The initial surface mesh consists of 9728 triangles and 4969 vertices with 208 vertices on the boundary, and the time step is uniformly chosen as $\tau = 10^{-4}$.

pinch-off phenomenon has often been identified as the Rayleigh-like instability [32, 44] governed by surface diffusion. To study this particular phenomenon for solid-state dewetting problems, we perform many numerical simulations with different initial islands given by different lengths of $(1, L, 1)$ cuboids. As shown in Figures 4.4 and 4.5, for an initial $(1, 12, 1)$ cuboid island with material constant $\sigma = \cos(3\pi/4)$, we can observe that the island evolves and breaks up into two small isolated islands,

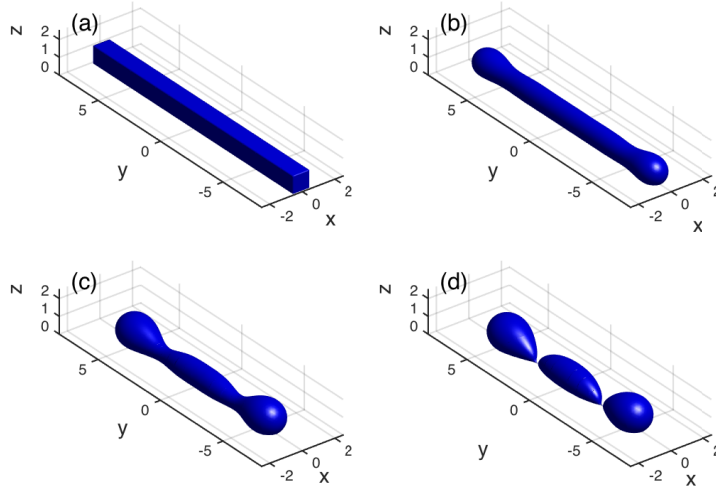


FIG. 4.5. Several snapshots in the evolution of an initial $(1, 16, 1)$ cuboid island until its pinch-off: (a) $t = 0$; (b) $t = 0.20$; (c) $t = 0.90$; (d) $t = 1.14$, where the material constant is chosen as $\sigma = \cos(3\pi/4)$. The initial surface mesh consists of 12800 triangles and 6537 vertices with 272 vertices on the boundary, and the time step is uniformly chosen as $\tau = 10^{-4}$.

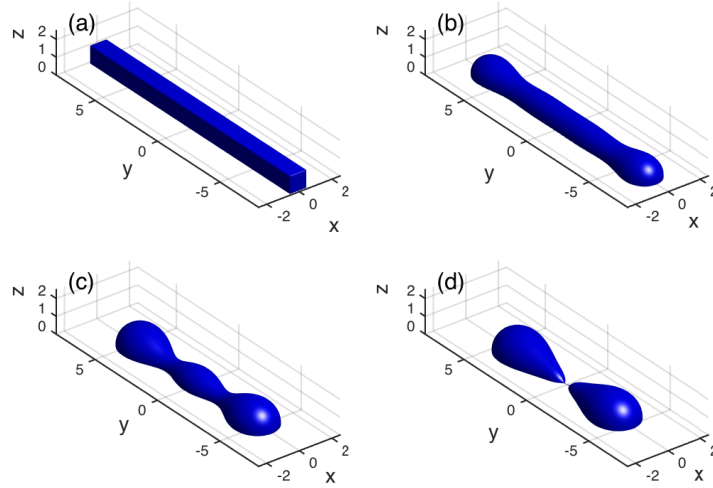


FIG. 4.6. Several snapshots in the evolution of an initial $(1, 16, 1)$ cuboid island until its pinch-off: (a) $t = 0$; (b) $t = 0.50$; (c) $t = 2.00$; (d) $t = 3.40$, where $\sigma = \cos(\pi/2)$. The initial surface mesh consists of 12800 triangles and 6537 vertices with 272 vertices on the boundary, and the time step is uniformly chosen as $\tau = 10^{-4}$.

and an initial $(1, 16, 1)$ cuboid island could break up into three pieces. Furthermore, by changing $\sigma = \cos(\pi/2)$, we observe that an initial $(1, 16, 1)$ cuboid island only breaks up into two small isolated islands (cf. Figure 4.6). This indicates that when σ increases, a cuboid island will become more difficult to pinch off.

From the above numerical simulations, we observe that there exist two critical lengths L_1, L_2 such that when $L_1 < L < L_2$, an initial $(1, L, 1)$ cuboid island will

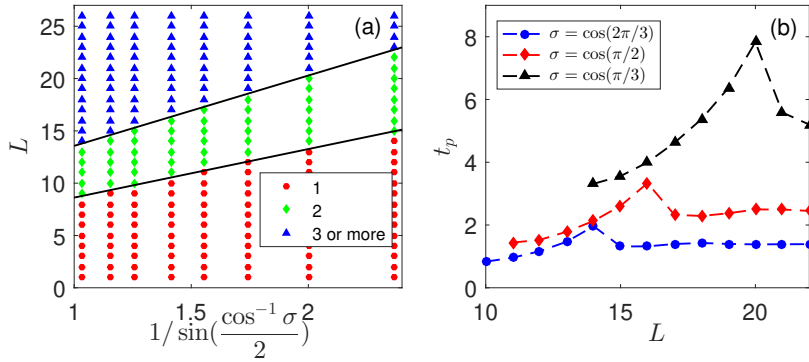


FIG. 4.7. (a) The number of islands formed from an initial $(1, L, 1)$ cuboid island with material constant σ , where the 1-2 islands' and 2-3 islands' boundaries (solid lines) are linear curve fittings to our numerical simulations given by $L = 3.98 + 4.64/\sin(\arccos \sigma/2)$ and $L = 6.84 + 6.73/\sin(\arccos \sigma/2)$. (b) The first pinch-off time t_p for an initial $(1, L, 1)$ cuboid island under three different material constants σ .

break up into two small isolated particles; and when $L > L_2$, the cuboid island will break up into three or more particles. Furthermore, we also observe that these two critical lengths are highly dependent on the material constant σ . By performing ample numerical simulations, as shown in Figure 4.7(a), we plot the phase diagram for the numbers of islands formed from an initial $(1, L, 1)$ cuboid island under different material constants σ . From the figure, we can observe that the critical lengths L_1 and L_2 both exhibit the reciprocal linear relationship with the variable $\sin(\arccos \sigma/2)$. We note that several similar relationships have also been observed and reported for the solid-state dewetting in 2D [49, 17]. Moreover, we plot the first pinch-off time t_p for an initial $(1, L, 1)$ cuboid island under three different material constants, i.e., $\sigma = \cos(\pi/3), \cos(\pi/2), \cos(2\pi/3)$. As shown in Figure 4.7(b), we can observe that when L increases, the first pinch-off time t_p first increases quickly to a maximum value and then decreases slowly to a constant. This is certainly reasonable because for an infinitely long $(1, L, 1)$ cuboid island, its first pinch-off time should be a constant which is only dependent on σ .

Motivated by recent experiments by Thompson's group [48, 57], we next numerically investigate morphology evolutions for island films initially with some special geometries, such as the cross shape and square-ring shape. In the following simulations, the height of the initial island film is always chosen to be 1, and the material constant is fixed at $\sigma = \cos(3\pi/4)$ unless otherwise stated.

To compare the evolution process with the recent experiments [48, 57], we first choose the initial geometry of the island film as a unit cube plus four equal limbs which are given by four $(1, L, 1)$ cuboids (shown in Figure 4.8(a)). We test two numerical examples with length parameters $L = 4$ and $L = 6$. As can be seen in Figure 4.8, when the limbs are chosen to be shorter (i.e., $L = 4$), we observe that the four limbs of the islands shrink, and then the cross-shaped island eventually evolves into a single island with spherical geometry as its equilibrium shape. However, when the four limbs are chosen to be longer (i.e., $L = 6$), the kinetic evolution of the island could be quite different. As depicted in Figure 4.9, instead of eventually forming a single spherical island, the cross-shaped island undergoes the pinch-off somewhere and finally breaks up into five small isolated solid particles.

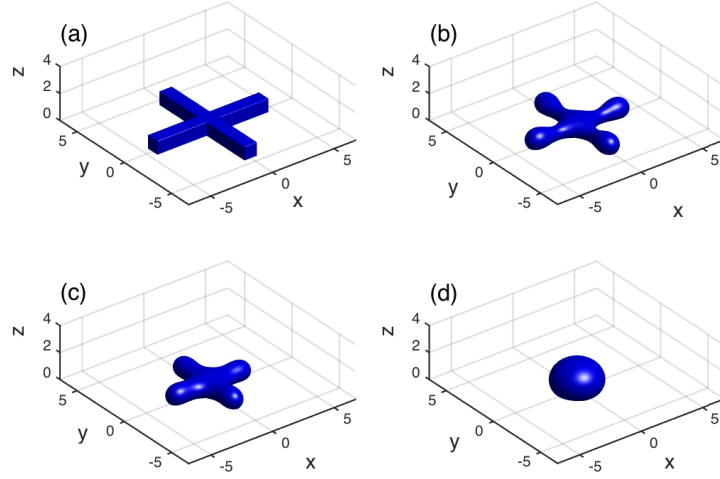


FIG. 4.8. Several snapshots in the evolution of an initially cross-shaped island towards its equilibrium, where the initial island consists of four $(1,4,1)$ cuboids forming the limbs and one $(1,1,1)$ cube sitting in the center: (a) $t = 0$; (b) $t = 0.15$; (c) $t = 0.50$; (d) $t = 1.40$. The initial surface mesh consists of 13568 triangles and 6929 vertices with 289 vertices on the boundary, and the time step is uniformly chosen as $\tau = 10^{-4}$.

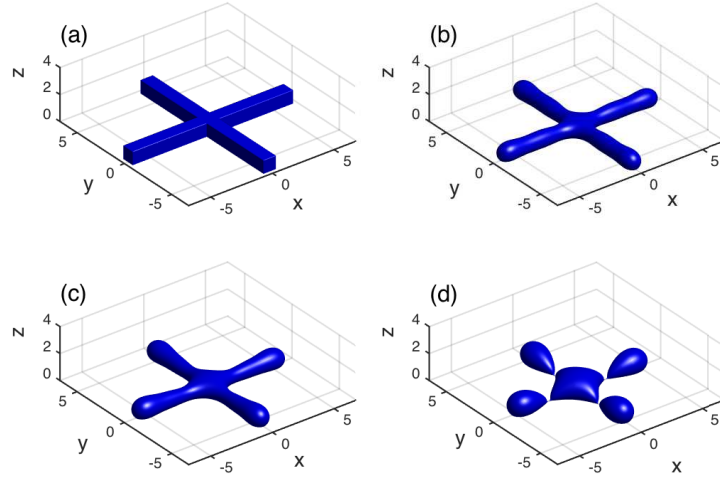


FIG. 4.9. Several snapshots in the evolution of an initially cross-shaped island before its pinch-off, where the initial island consists of four $(1,6,1)$ cuboids forming the limbs and one $(1,1,1)$ cube sitting in the center: (a) $t = 0$; (b) $t = 0.05$; (c) $t = 0.15$; (d) $t = 0.386$. The initial surface mesh consists of 19712 triangles and 10065 vertices with 416 vertices on the boundary, and the time step is uniformly chosen as $\tau = 10^{-4}$.

We next consider the evolution of an island film which is initially chosen as a square-ring shape. First, we choose an initial “fat” square-ring island, which is given by a $(5, 5, 1)$ cuboid by cutting out a $(3, 3, 1)$ cuboid from the center (shown in Figure 4.10). Its geometry evolution together with the cross-section profile of the island are shown in Figure 4.10 and Figure 4.11, respectively. From these figures, we clearly

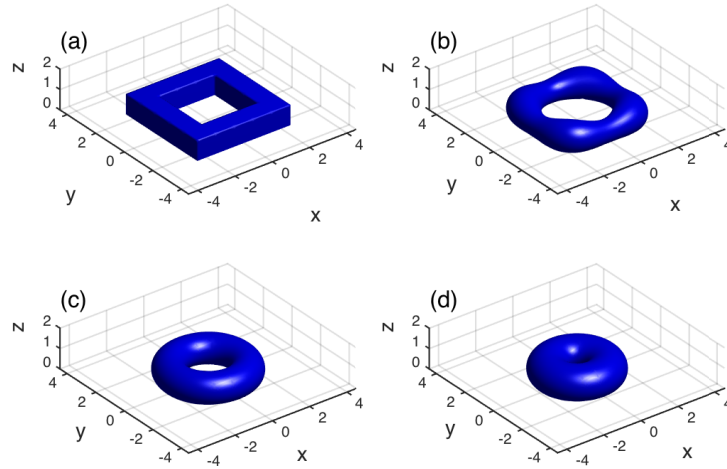


FIG. 4.10. Several snapshots in the evolution of an initial island of square-ring obtained from a $(5, 5, 1)$ cuboid by cutting out a $(3, 3, 1)$ cuboid from the center: (a) $t = 0$; (b) $t = 0.15$; (c) $t = 1.00$; (d) $t = 1.50$. The initial surface mesh consists of 12288 triangles and 6272 vertices with 96 and 160 vertices for the inner and outer contact lines, respectively, and the time step is uniformly chosen as $\tau = 5 \times 10^{-4}$.

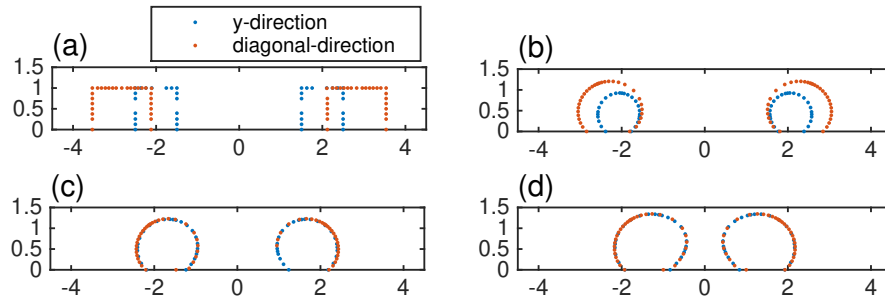


FIG. 4.11. The corresponding cross-section profiles of the island geometry in the evolution shown in Figure 4.10: (a) $t = 0$; (b) $t = 0.15$; (c) $t = 1.00$; (d) $t = 1.50$.

observe that the square-ring island quickly evolves into a ring-like shape with different thickness along different cross-section directions (see Figure 4.11(b)). Subsequently, as time evolves, this ring-like shape evolves into a toroidal shape (i.e., its thickness is the same along each cross-section direction) (see Figure 4.11(c)); then the toroidal island shrinks towards the center in order to reduce the total free energy.

Furthermore, if we choose an initial “thin” square-ring island (i.e., enlarge the length of outer edge of the island, while fixing the inner width of the square-ring island as 1), the pinch-off events will occur as expected due to Rayleigh-like instability, as shown in Figures 4.12 and 4.13. Figure 4.12 depicts the morphology evolution and contact line migration (including inner and outer contact lines) when the length of the outer edge is chosen as 7. From this figure, we clearly see that the inner width of the island very quickly becomes wavy along its different azimuthal directions; and as time evolves, the place where its inner width is thick becomes thicker and thicker, while the place where it is thin becomes thinner and thinner. Finally, when the width

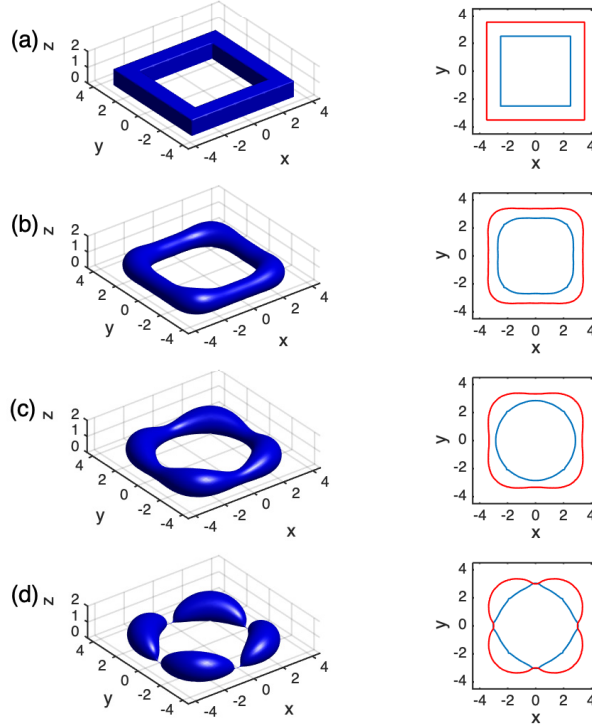


FIG. 4.12. Several snapshots in the evolution of an initial square-ring island obtained from a $(7, 7, 1)$ cuboid by cutting out a $(5, 5, 1)$ cuboid from the center: (a) $t = 0$; (b) $t = 0.15$; (c) $t = 0.40$; (d) $t = 0.61$.

of the thin place approaches zero, the pinch-off events will happen such that it breaks up into four small particles. On the other hand, if we continue to enlarge the length of outer edge (e.g., choose it as 12), as shown in Figure 4.13, we can observe that the square-ring island will finally split into eight small particles.

From the above numerical simulations, we can observe that the Rayleigh-like instability in the azimuthal direction and the shrinking instability in the radial direction are competing with each other to determine the solid-state dewetting evolution of a square-ring island. This is a competition between the two time scales: one for toroid shrinkage towards its center and the other for neck pinch-off along the azimuthal direction. When the square-ring island is very thin (shown in Figures 4.12 and 4.13), the Rayleigh-like instability dominates its kinetic evolution and makes the island break up into small isolated particles; when it is very fat (shown in Figure 4.10), the shrinking instability dominates the evolution and makes it shrink towards the center. The shrinking instability for a toroidal island on a substrate has been studied in [31, 58] under the assumption of axis-symmetric geometry. But it is still an open problem about quantitatively studying the competition effect by a simultaneous consideration of the shrinking instability and Rayleigh-like instability. Our proposed approach could be a good avenue for exploring this problem.

4.3. For the weakly anisotropic case. In this subsection, we perform some numerical simulations to investigate solid-state dewetting of thin films with anisotropic

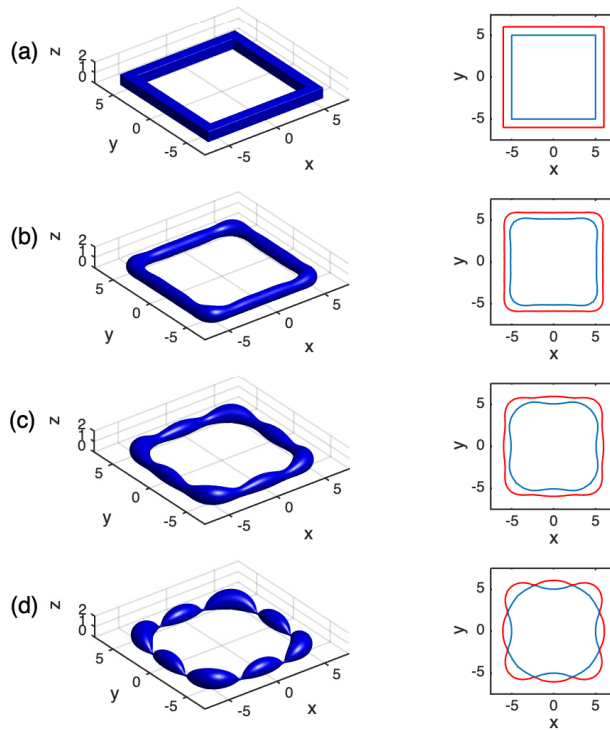


FIG. 4.13. Several snapshots in the evolution of an initial square-ring island obtained from a $(12, 12, 1)$ cuboid by cutting out a $(10, 10, 1)$ cuboid from the center: (a) $t = 0$; (b) $t = 0.15$; (c) $t = 0.70$; (d) $t = 1.00$.

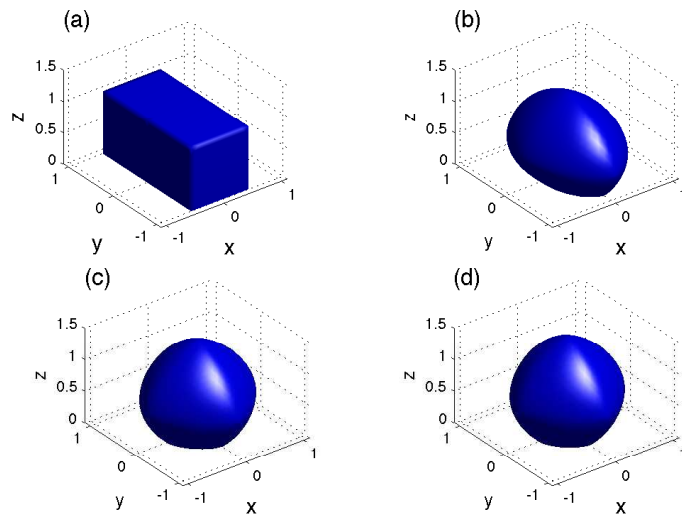


FIG. 4.14. Several snapshots in the evolution of an initially $(1, 2, 1)$ cuboid island towards its equilibrium under the cubic anisotropy with $a = 0.3$: (a) $t = 0$; (b) $t = 0.02$; (c) $t = 0.10$; (d) $t = 0.21$, where $\sigma = \cos(5\pi/6)$, and the initial surface mesh consists of 2048 triangles and 1049 vertices with 48 vertices on the boundary, and the time step is uniformly chosen as $\tau = 10^{-4}$.

surface energies. We first focus on the following cubic anisotropy:

$$(4.2) \quad \gamma(\mathbf{n}) = 1 + a[n_1^4 + n_2^4 + n_3^4], \quad -\frac{2}{9} < a < \frac{1}{3},$$

where a represents the degree of the anisotropy.

We start the numerical experiment for an initial $(1, 2, 1)$ cuboid island. The surface energy is chosen as the cubic anisotropy with $a = 0.3$, and the material constant is chosen as $\sigma = \cos(5\pi/6)$. Several snapshots of the morphology evolution of the island film are shown in Figure 4.14. From the figure, we can observe that the island film evolves towards a nonspherical shape with “sharp” corners.

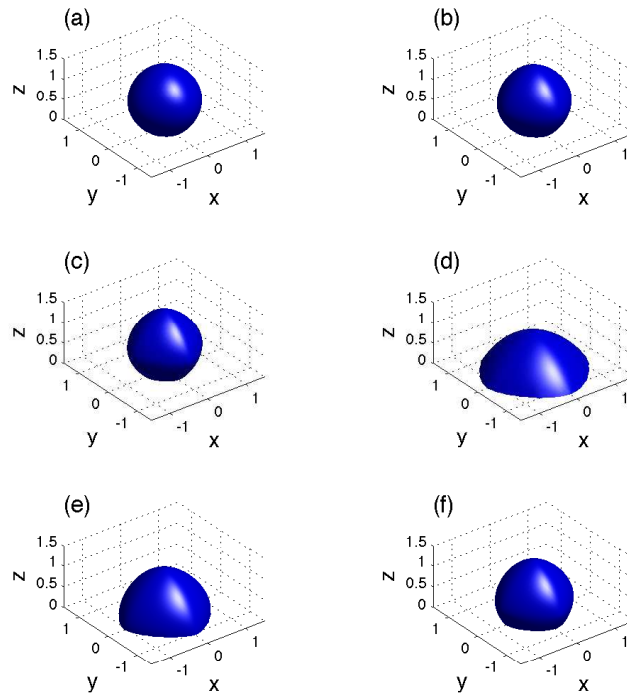


FIG. 4.15. The equilibrium geometry of islands under the cubic anisotropy with different material constants σ . From (a)–(c), the material constant is fixed as $\sigma = \cos(5\pi/6)$, and the degrees of anisotropy are chosen as $a = 0.1, 0.2, 0.3$; from (d)–(f), the degree of anisotropy is fixed at $a = 0.3$, and the material constants are chosen as $\sigma = \cos(\pi/3), \cos(\pi/2), \cos(2\pi/3)$.

By performing numerical simulations, we next examine the equilibrium geometry under different degrees of cubic anisotropy and different material constants. As clearly shown in Figure 4.15(a)–(c), when the degree of the anisotropy is increased from 0.1 to 0.3 with a material constant $\sigma = \cos(5\pi/6)$, the equilibrium shape exhibits increasingly sharper and sharper corners. Furthermore, from Figure 4.15(d)–(f), when we change the value of the material constant, we also clearly observe the corresponding change in its equilibrium shape.

Under the cubic surface energy, as expected, the long island film will also exhibit Rayleigh-like instability and could pinch off into small pieces of islands. We consider the evolution of an initial $(1, 12, 1)$ cuboid island, and the degree of the cubic surface energy is chosen as $a = 0.25$, and the material constant is chosen as $\sigma = \cos(2\pi/3)$.

As can be seen in Figure 4.16, the long cuboid island pinches off, and finally dewets to three pieces of small islands.

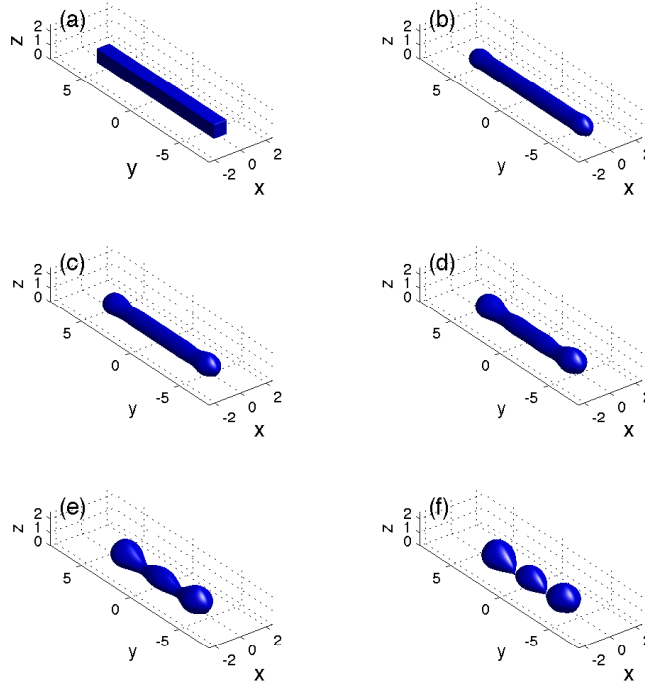


FIG. 4.16. Several snapshots in the evolution of an initially $(1, 12, 1)$ cuboid island until its pinch-off under the cubic anisotropy with $a = 0.25$: (a) $t = 0$; (b) $t = 0.30$; (c) $t = 0.60$; (d) $t = 0.90$; (e) $t = 1.40$; (f) $t = 1.58$. The material constant is chosen as $\sigma = \cos(2\pi/3)$.

In addition to the cubic anisotropy, we also perform numerical simulations for the ellipsoidal anisotropy, which is defined as

$$(4.3) \quad \gamma(\mathbf{n}) = \sqrt{a_1^2 n_1^2 + a_2^2 n_2^2 + a_3^2 n_3^2},$$

where a_1, a_2, a_3 are the ratios in each direction component. The corresponding equilibrium shape for this type of anisotropy is self-similar to an ellipsoid with semimajor axes a_1, a_2, a_3 (see [30]), i.e.,

$$(4.4) \quad \frac{x^2}{a_1^2} + \frac{y^2}{a_2^2} + \frac{z^2}{a_3^2} = 1.$$

Figure 4.17 depicts the morphology evolution of an initial cuboid island towards its equilibrium shape. The surface energy anisotropy is chosen as $\gamma(\mathbf{n}) = \sqrt{2n_1^2 + n_2^2 + n_3^2}$. From the figure, we can see that the island film eventually reaches its equilibrium with an ellipsoidal shape. This is consistent with the theoretical prediction since the corresponding equilibrium shape for the anisotropy $\gamma(\mathbf{n}) = \sqrt{2n_1^2 + n_2^2 + n_3^2}$ is self-similar to an ellipsoid $\frac{x^2}{2} + y^2 + z^2 = 1$.

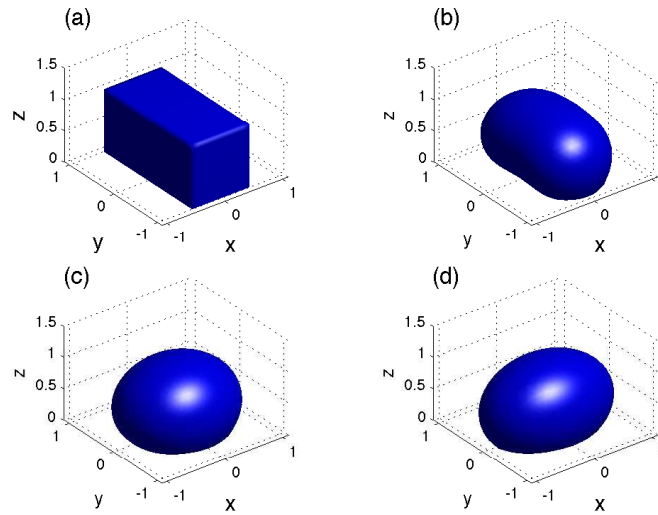


FIG. 4.17. Several snapshots in the evolution of an initially $(1, 2, 1)$ cuboid island towards its equilibrium under the ellipsoidal anisotropy with $a_1 = \sqrt{2}, a_2 = 1, a_3 = 1$: (a) $t = 0$; (b) $t = 0.01$; (c) $t = 0.05$; (d) $t = 0.20$, where the material constant is chosen as $\sigma = \cos(3\pi/4)$, and the initial surface mesh consists of 2048 triangles and 1049 vertices with 48 vertices on the boundary, and the time step is uniformly chosen as $\tau = 10^{-4}$.

5. Conclusions. Based on a novel variational formulation in terms of ξ -vector formulation, we developed a parametric finite element method (PFEM) for solving solid-state dewetting problems in three dimensions (3D). In each time step, the contact line Γ^{m+1} is first updated according to the relaxed contact angle condition; then, by prescribing the boundary curve Γ^{m+1} as the explicit boundary condition, the variational formulation is discretized by a semi-implicit PFEM in order to obtain the new surface S^{m+1} . The resulting system is a system of linear and sparse algebra equations which can be efficiently solved by many existing fast algorithms. We performed ample numerical examples for investigating solid-state dewetting of thin films with isotropic/weakly anisotropic surface energies. We observed that small islands tend to form spherical shapes as the equilibrium in the isotropic case, while long islands could break up into pieces of small isolated islands, and islands with some special geometries exhibit interesting phenomena and complexities. Numerical results have demonstrated high efficiency and accuracy of the proposed PFEM scheme for solving solid-state dewetting problems with isotropic/weakly anisotropic surface energies in 3D.

REFERENCES

- [1] D. AMRAM, L. KLINGER, AND E. RABKIN, *Anisotropic hole growth during solid-state dewetting of single-crystal Au–Fe thin films*, Acta Mater., 60 (2012), pp. 3047–3056.
- [2] E. BÄNSCH, P. MORIN, AND R. H. NOCHETTO, *Surface diffusion of graphs: Variational formulation, error analysis, and simulation*, SIAM J. Numer. Anal., 42 (2004), pp. 773–799, <https://doi.org/10.1137/S0036142902419272>.
- [3] E. BÄNSCH, P. MORIN, AND R. H. NOCHETTO, *A finite element method for surface diffusion: The parametric case*, J. Comput. Phys., 203 (2005), pp. 321–343.
- [4] W. BAO, W. JIANG, D. J. SROLOVITZ, AND Y. WANG, *Stable equilibria of anisotropic particles on substrates: A generalized Winterbottom construction*, SIAM J. Appl. Math., 77 (2017), pp. 2093–2118, <https://doi.org/10.1137/16M1091599>.

- [5] W. BAO, W. JIANG, Y. WANG, AND Q. ZHAO, *A parametric finite element method for solid-state dewetting problems with anisotropic surface energies*, *J. Comput. Phys.*, 330 (2017), pp. 380–400.
- [6] J. W. BARRETT, H. GARCKE, AND R. NÜRNBERG, *Numerical approximation of anisotropic geometric evolution equations in the plane*, *IMA J. Numer. Anal.*, 28 (2007), pp. 292–330.
- [7] J. W. BARRETT, H. GARCKE, AND R. NÜRNBERG, *On the variational approximation of combined second and fourth order geometric evolution equations*, *SIAM J. Sci. Comput.*, 29 (2007), pp. 1006–1041, <https://doi.org/10.1137/060653974>.
- [8] J. W. BARRETT, H. GARCKE, AND R. NÜRNBERG, *A parametric finite element method for fourth order geometric evolution equations*, *J. Comput. Phys.*, 222 (2007), pp. 441–467.
- [9] J. W. BARRETT, H. GARCKE, AND R. NÜRNBERG, *On the parametric finite element approximation of evolving hypersurfaces in \mathbb{R}^3* , *J. Comput. Phys.*, 227 (2008), pp. 4281–4307.
- [10] J. W. BARRETT, H. GARCKE, AND R. NÜRNBERG, *Parametric approximation of Willmore flow and related geometric evolution equations*, *SIAM J. Sci. Comput.*, 31 (2008), pp. 225–253, <https://doi.org/10.1137/070700231>.
- [11] J. W. BARRETT, H. GARCKE, AND R. NÜRNBERG, *A variational formulation of anisotropic geometric evolution equations in higher dimensions*, *Numer. Math.*, 109 (2008), pp. 1–44.
- [12] J. W. BARRETT, H. GARCKE, AND R. NÜRNBERG, *Finite-element approximation of coupled surface and grain boundary motion with applications to thermal grooving and sintering*, *European J. Appl. Math.*, 21 (2010), pp. 519–556.
- [13] J. CAHN AND D. HOFFMAN, *A vector thermodynamics for anisotropic surfaces: I. Curved and faceted surfaces*, *Acta Metall.*, 22 (1974), pp. 1205–1214.
- [14] J. W. CAHN AND J. E. TAYLOR, *Surface motion by surface diffusion*, *Acta Metall. Mater.*, 42 (1994), pp. 1045–1063.
- [15] P.-G. DE GENNES, *Wetting: Statics and dynamics*, *Rev. Mod. Phys.*, 57 (1985), pp. 827–863.
- [16] K. DECKELNICK, G. DZIUK, AND C. M. ELLIOTT, *Computation of geometric partial differential equations and mean curvature flow*, *Acta Numer.*, 14 (2005), pp. 139–232.
- [17] E. DORNEL, J. BARBE, F. DE CRÉCY, G. LACOLLE, AND J. EYMER, *Surface diffusion dewetting of thin solid films: Numerical method and application to Si/SiO₂*, *Phys. Rev. B*, 73 (2006), 115427.
- [18] P. DU, M. KHENNER, AND H. WONG, *A tangent-plane marker-particle method for the computation of three-dimensional solid surfaces evolving by surface diffusion on a substrate*, *J. Comput. Phys.*, 229 (2010), pp. 813–827.
- [19] G. DZIUK, *An algorithm for evolutionary surfaces*, *Numer. Math.*, 58 (1990), pp. 603–611.
- [20] G. DZIUK AND C. M. ELLIOTT, *Finite element methods for surface PDEs*, *Acta Numer.*, 22 (2013), pp. 289–396.
- [21] F. HAUSSER AND A. VOIGT, *A discrete scheme for regularized anisotropic surface diffusion: A 6th order geometric evolution equation*, *Interfaces Free Bound.*, 7 (2005), pp. 353–370.
- [22] F. HAUSSER AND A. VOIGT, *A discrete scheme for parametric anisotropic surface diffusion*, *J. Sci. Comput.*, 30 (2007), pp. 223–235.
- [23] S. HILDEBRANDT AND H. KARCHER, *Geometric Analysis and Nonlinear Partial Differential Equations*, Springer, Berlin, 2003.
- [24] D. W. HOFFMAN AND J. W. CAHN, *A vector thermodynamics for anisotropic surfaces: I. Fundamentals and application to plane surface junctions*, *Surface Sci.*, 31 (1972), pp. 368–388.
- [25] S. Y. HON, S. LEUNG, AND H. ZHAO, *A cell based particle method for modeling dynamic interfaces*, *J. Comput. Phys.*, 272 (2014), pp. 279–306.
- [26] Q.-A. HUANG, W. JIANG, AND J. Z. YANG, *An efficient and unconditionally energy stable scheme for simulating solid-state dewetting of thin films with isotropic surface energy*, *Commun. Comput. Phys.*, 26 (2019), pp. 1444–1470.
- [27] W. JIANG, W. BAO, C. V. THOMPSON, AND D. J. SROLOVITZ, *Phase field approach for simulating solid-state dewetting problems*, *Acta Mater.*, 60 (2012), pp. 5578–5592.
- [28] W. JIANG, Y. WANG, Q. ZHAO, D. J. SROLOVITZ, AND W. BAO, *Solid-state dewetting and island morphologies in strongly anisotropic materials*, *Scripta Mater.*, 115 (2016), pp. 123–127.
- [29] W. JIANG AND Q. ZHAO, *Sharp-interface approach for simulating solid-state dewetting in two dimensions: A Cahn-Hoffman ξ -vector formulation*, *Phys. D*, 390 (2019), pp. 69–83.
- [30] W. JIANG, Q. ZHAO, AND W. BAO, *Sharp-Interface Approach for Simulating Solid-State Dewetting in Three Dimensions*, preprint, <https://arxiv.org/abs/1902.05272>, 2019.
- [31] W. JIANG, Q. ZHAO, T. QIAN, D. J. SROLOVITZ, AND W. BAO, *Application of Onsager's variational principle to the dynamics of a solid toroidal island on a substrate*, *Acta Mater.*, 163 (2019), pp. 154–160.

- [32] G. H. KIM AND C. V. THOMPSON, *Effect of surface energy anisotropy on Rayleigh-like solid-state dewetting and nanowire stability*, *Acta Mater.*, 84 (2015), pp. 190–201.
- [33] G. H. KIM, R. V. ZUCKER, J. YE, W. C. CARTER, AND C. V. THOMPSON, *Quantitative analysis of anisotropic edge retraction by solid-state dewetting of thin single crystal films*, *J. Appl. Phys.*, 113 (2013), 043512.
- [34] O. KOVALENKO, S. SZABÓ, L. KLINGER, AND E. RABKIN, *Solid state dewetting of polycrystalline Mo film on sapphire*, *Acta Mater.*, 139 (2017), pp. 51–61.
- [35] F. LEROY, L. BOROWIK, F. CHEYNIS, Y. ALMADORI, S. CURIOTTO, M. TRAUTMANN, J. BARBÉ, AND P. MÜLLER, *How to control solid state dewetting: A short review*, *Surface Sci. Rep.*, 71 (2016), pp. 391–409.
- [36] S. LEUNG, J. LOWENGRUB, AND H. ZHAO, *A grid based particle method for solving partial differential equations on evolving surfaces and modeling high order geometrical motion*, *J. Comput. Phys.*, 230 (2011), pp. 2540–2561.
- [37] J. MIZSEI, *Activating technology of SnO₂ layers by metal particles from ultrathin metal films*, *Sensors Actuators B Chem.*, 16 (1993), pp. 328–333.
- [38] W. W. MULLINS, *Theory of thermal grooving*, *J. Appl. Phys.*, 28 (1957), pp. 333–339.
- [39] M. NAFFOUTI, T. DAVID, A. BENKOUDER, L. FAVRE, A. DELOBBE, A. RONDA, I. BERBEZIER, AND M. ABBARCHI, *Templated solid-state dewetting of thin silicon films*, *Small*, 12 (2016), pp. 6115–6123.
- [40] P. POZZI, *Anisotropic mean curvature flow for two-dimensional surfaces in higher codimension: A numerical scheme*, *Interface Free Bound.*, 10 (2008), pp. 539–576.
- [41] T. QIAN, X.-P. WANG, AND P. SHENG, *A variational approach to moving contact line hydrodynamics*, *J. Fluid Mech.*, 564 (2006), pp. 333–360.
- [42] E. RABKIN, D. AMRAM, AND E. ALSTER, *Solid state dewetting and stress relaxation in a thin single crystalline Ni film on sapphire*, *Acta Mater.*, 74 (2014), pp. 30–38.
- [43] S. RANDOLPH, J. FOWLKES, A. MELECHKO, K. KLEIN, H. MEYER, III, M. SIMPSON, AND P. RACK, *Controlling thin film structure for the dewetting of catalyst nanoparticle arrays for subsequent carbon nanofiber growth*, *Nanotechnology*, 18 (2007), 465304.
- [44] L. RAYLEIGH, *On the instability of jets*, *Proc. Lond. Math. Soc.*, 10 (1878/79), pp. 4–13.
- [45] V. SCHMIDT, J. V. WITTEMANN, S. SENZ, AND U. GÖSELE, *Silicon nanowires: A review on aspects of their growth and their electrical properties*, *Adv. Mater.*, 21 (2009), pp. 2681–2702.
- [46] D. J. SROLOVITZ AND S. A. SAFRAN, *Capillary instabilities in thin films: I. Energetics*, *J. Appl. Phys.*, 60 (1986), pp. 247–254.
- [47] J. E. TAYLOR, *II-mean curvature and weighted mean curvature*, *Acta Metall. Mater.*, 40 (1992), pp. 1475–1485.
- [48] C. V. THOMPSON, *Solid-state dewetting of thin films*, *Annu. Rev. Mater. Res.*, 42 (2012), pp. 399–434.
- [49] Y. WANG, W. JIANG, W. BAO, AND D. J. SROLOVITZ, *Sharp interface model for solid-state dewetting problems with weakly anisotropic surface energies*, *Phys. Rev. B*, 91 (2015), 045303.
- [50] W. WINTERBOTTOM, *Equilibrium shape of a small particle in contact with a foreign substrate*, *Acta Metall.*, 15 (1967), pp. 303–310.
- [51] H. WONG, P. VOORHEES, M. MIKSIS, AND S. DAVIS, *Periodic mass shedding of a retracting solid film step*, *Acta Mater.*, 48 (2000), pp. 1719–1728.
- [52] X. XU AND X. WANG, *Derivation of the Wenzel and Cassie equations from a phase field model for two phase flow on rough surface*, *SIAM J. Appl. Math.*, 70 (2010), pp. 2929–2941, <https://doi.org/10.1137/090775828>.
- [53] X. XU AND X. WANG, *Analysis of wetting and contact angle hysteresis on chemically patterned surfaces*, *SIAM J. Appl. Math.*, 71 (2011), pp. 1753–1779, <https://doi.org/10.1137/110829593>.
- [54] Y. XU AND C.-W. SHU, *Local discontinuous Galerkin method for surface diffusion and Willmore flow of graphs*, *J. Sci. Comput.*, 40 (2009), pp. 375–390.
- [55] J. YE AND C. V. THOMPSON, *Regular pattern formation through the retraction and pinch-off of edges during solid-state dewetting of patterned single crystal films*, *Phys. Rev. B*, 82 (2010), 193408.
- [56] J. YE AND C. V. THOMPSON, *Anisotropic edge retraction and hole growth during solid-state dewetting of single crystal nickel thin films*, *Acta Mater.*, 59 (2011), pp. 582–589.
- [57] J. YE AND C. V. THOMPSON, *Templated solid-state dewetting to controllably produce complex patterns*, *Adv. Mater.*, 23 (2011), pp. 1567–1571.
- [58] Q. ZHAO, *A sharp-interface model and its numerical approximation for solid-state dewetting with axisymmetric geometry*, *J. Comput. Appl. Math.*, 361 (2019), pp. 144–156.

- [59] Q. ZHAO, W. JIANG, D. J. SROLOVITZ, AND W. BAO, *Triple junction drag effects during topological changes in the evolution of polycrystalline microstructures*, Acta Mater., 128 (2017), pp. 345–350.
- [60] R. V. ZUCKER, G. H. KIM, J. YE, W. C. CARTER, AND C. V. THOMPSON, *The mechanism of corner instabilities in single-crystal thin films during dewetting*, J. Appl. Phys., 119 (2016), 125306.